Controls on Wintertime Nonbrightband Rain Rate and Frequency in California's Northern Coast Ranges

MATTHEW D. CANN[a] AND ALLEN B. WHITE[b]

[a] *Department of Atmospheric and Oceanic Sciences, University of Colorado Boulder, Boulder, Colorado*
[b] *NOAA/Earth System Research Laboratory/Physical Sciences Laboratory, Boulder, Colorado*

(Manuscript received 18 February 2020, in final form 21 April 2021)

ABSTRACT: Nonbrightband (NBB) rain is a shallow, orographic precipitation that does not produce a radar bright band as a result of melting ice crystals. However, NBB rain is not the same as warm rain, which excludes ice from being involved in the microphysical growth of precipitation. Despite this difference, NBB rain is often treated as warm rain in the literature, and past studies have mostly ignored the role of ice. Here, we use two wet seasons (2015/16 and 2016/17) at four precipitation-observing sites in the Northern Coast Ranges of California to show the role of echo top height and ice in determining NBB rain intensity. It was found that NBB rain was only absent of bright bands 32%–46% of the time depending on location of the site. Additionally, all NBB rain rates that exceeded 10 mm h^{-1} exhibited observable bright bands during the hour period. We also define growth efficiency (GE) as the ability of shallow rain clouds to produce raindrops larger than drizzle size ($D > 0.5$ mm). High-GE rain drop size distributions were composed of fewer small drops and more large drops than low-GE rain, which was mostly drizzle. High-GE rain occurred with echo top heights above the freezing level where rapid growth of precipitation was observed by radar. Echo tops that only extended 1 km or less above the freezing level suggested hydrometeor growth from mixed-phase processes, indicating that ice may be present in coastal precipitation at warmer temperatures than previously considered.

KEYWORDS: Rainfall; Cloud microphysics; Coastal meteorology; Hydrometeorology; Mesoscale processes; Orographic effects

1. Introduction

In the past two decades, studies have regarded coastal precipitation that does not produce a bright band from melting ice crystals, or nonbrightband (NBB) rain, as a warm-rain dominated process. Understanding the controls on NBB rain intensity and frequency are crucial in California where NBB rain can produce as much as 50% of the annual wet season (November–March) precipitation in the flood-prone Northern Coast Ranges (White et al. 2015). Moreover, precipitation in California is often feast or famine, frequently translating into disastrous floods or lingering drought conditions (Ralph et al. 2006; Dettinger et al. 2011; Rosen 2017; Lund et al. 2018). Vertically pointing radars allow for easy identification of NBB rain, which is typically shallow and often undetectable by conventional WSR-88D scanning radar (White et al. 2003; Matrosov et al. 2014). Previous studies were confined to one or two vertically pointing radar sites in the Northern Coast Ranges and therefore limited in their geographic variability at the small scale (White et al. 2003, 2015; Neiman et al. 2005; Kingsmill et al. 2006, 2016; Martner et al. 2008). This study extends the latitudinal and altitudinal ranges of NBB rain observations in the Northern Coast Ranges by introducing new valley and mountain sites. Additionally, past work has shown that upslope wind speed and integrated water vapor (IWV) are correlated to rain rates at a mountain site in the Northern Coast Ranges (Neiman et al. 2002, 2009; Kingsmill et al. 2016). Here, we evaluate these variables along with echo top heights and explore the role of ice in NBB rain intensity through brightband percentages and freezing levels heights to demonstrate that ice is crucial for heavier NBB rain.

First, it is important to clearly distinguish between NBB rain and warm rain. As stated in White et al. (2003), "NBB rain is a shallow rainfall process which does not produce a detectable bright band, suggesting that ice microphysics does not play a dominant role in the precipitation process." Alternatively, warm rain must exclude ice-phase microphysics and form solely via the liquid-phase processes of condensation into cloud droplets and then collision–coalescence into drizzle and raindrops (Song and Marwitz 1989; Franklin 2008). Therefore, all warm rain events are inherently NBB rain, however, not all NBB rain can be considered warm rain. Despite this technical difference, studies colloquially refer to NBB rain as warm rain, separating it from ice-initiated rain (e.g., Kingsmill et al. 2016; Massmann et al. 2017). The way that NBB rain is classified in studies suggests that terming it "warm rain" is an oversimplification. Most studies employ a 50% precipitation profile threshold from vertically pointing radar in a given time period: when ≥50% of precipitation profiles exhibit a bright band it is termed brightband (BB) rain, and when <50% it is termed NBB rain (White et al. 2003; Neiman et al. 2005; Martner et al. 2008; Kingsmill et al. 2016; Massmann et al. 2017; Zagrodnik et al. 2018). Note that White et al. (2003) also employed a more stringent 20% threshold on NBB rain. Thus, in most studies, up to 49% of precipitation profiles in NBB rain actually contain bright bands. These definitions of NBB rain raise some intriguing questions: How much NBB rain occurs without any bright bands? And does the observed brightband percentage limit NBB rain intensity? These questions will be addressed in this study.

Corresponding author: Matthew D. Cann, matthew.cann@colorado.edu

DOI: 10.1175/JHM-D-20-0046.1

NBB rain is most common in coastal regions due to environmental conditions and aerosol content that promote the formation and fallout of precipitation from shallow clouds. NBB rain has been observed in the Coast Ranges and Sierra Nevada of California (White et al. 2003, 2015; Martner et al. 2008; Coplen et al. 2015; Kingsmill et al. 2016), the Oregon Cascades and Washington Olympics (Neiman et al. 2005; Zagrodnik et al. 2018), the Appalachian Mountains in the southeastern United States (Matrosov et al. 2016), and the Nahuelbuta Mountains of coastal Chile (Massmann et al. 2017). While NBB rain likely occurs in other regions of the world, the aforementioned locations are all midlatitude mountain ranges where warm, moist air is forced over near-coastal terrain to produce shallow orographic clouds. These clouds are most efficient in producing precipitation when cloud droplets are different sizes with inherently different fall speeds that promote collision–coalescence. Coastal regions with maritime flow offer a wide range of aerosol sizes including the presence of giant cloud condensation nuclei ($r > 2\,\mu$m) that can substantially improve the efficiency of collision–coalescence by rapidly producing large drops (Johnson 1982; Szumowski et al. 1997; Feingold et al. 1999; Whiteman 2000; Zhang et al. 2006; Posselt and Lohmann 2008; Jensen and Nugent 2017). A particularly important giant cloud condensation nuclei is sea-salt aerosols which typically produce concentrated salt solutions upon condensation and rapidly grow to precipitation size (Jensen and Nugent 2017). Sea-salt aerosols have been used to partially explain areas of higher NBB rain frequency in the Sierra Nevada and are shown in abundance in the Northern Coast Ranges (White et al. 2015). Lesser studied, and mainly in laboratory settings, is the ability of biological components to attach to sea-salt aerosols which can act as ice nucleating particles at temperatures of −5°C, or possibly warmer, and may account for high ice particle concentrations observed in maritime clouds with relatively warm tops (−5°C; Wallace and Hobbs 2006, and references therein; Wilson et al. 2015; DeMott et al. 2016; Ladino et al. 2016; Kanji et al. 2017, and references therein). The results of these studies imply that ice particles may be present in NBB rain clouds that extend only marginally above the freezing level, and that ice may play a more significant role than previously considered.

Even though ice may be present in both BB and NBB rain, they differ in numerous ways, while the atmospheric conditions that lead to their existence often occur simultaneously. BB rain is typically the result of synoptically forced midtropospheric ascent, whereas NBB rain is commonly produced by mesoscale orographic lift of shallow, moist air (Neiman et al. 2005; Massmann et al. 2017). When BB rain continues to enhance beneath the bright band by the shallow physical processes that induce NBB rain, it is further termed hybrid rain (White et al. 2003). At many observing sites, hybrid rain is more common than BB rain (e.g., White et al. 2003, 2015; Neiman et al. 2005; Kingsmill et al. 2006) due to NBB rain often manifesting itself in the background while overrun by deeper BB rain (e.g., Figs. 2–4 in Neiman et al. 2005). NBB rain is common during warm frontal passage, the warm sector, and post-cold-frontal cool sector, and relatively absent in the pre-warm-frontal cold sector due to lack of warm moist flow and during cold frontal passage due to midtropospheric ascent forcing hybrid rainfall (Neiman et al. 2005; Kingsmill et al. 2006). Both BB and NBB rain intensities are correlated to low-level orographic forcing (Kingsmill et al. 2016; Massmann et al. 2017). Total hourly rainfall in the Northern Coast Ranges is weakly correlated to IWV, more strongly correlated with low-level upslope flow, with marginal improvements when the two forcing mechanisms are combined into upslope water vapor flux (Neiman et al. 2002, 2009; Kingsmill et al. 2016). However, Kingsmill et al. (2016) found that when rainfall hours are divided by type, the addition of IWV is negligible or even reduces the correlation with rainfall rate. NBB rain rate is also less correlated to IWV than BB rain rate, and in a 10-yr composite, the heaviest NBB rain fell with IWV between 2 and 3 cm rather than 3+ cm (Kingsmill et al. 2016). The unique relationship between IWV and NBB rain rate will be addressed in this study.

In addition to synoptic versus orographic forcing, differences in NBB and BB rain can also be observed at the surface using disdrometers. NBB rain is typically dominated by larger concentrations of small drops and few large drops whereas BB rain exhibits more large drops with fewer total drops (Martner et al. 2008; Massmann et al. 2017). In hybrid rain where both mixed- and warm-phase processes are relevant for precipitation production, many large drops may exist along with an abundance of smaller drops, often leading to heavy rainfall (Friedrich et al. 2016; Zagrodnik et al. 2018, 2019).

This study utilizes data from four precipitation-observing sites with higher spatial density in the Northern Coast Ranges than previously studied for NBB rain and a coastal atmospheric monitoring site over two active wet seasons (2015/16, 2016/17). These data were used to address the following objectives:

- to understand NBB rain rate and frequency from high spatial density precipitation profilers in varying geographic locations in the Northern Coast Ranges of California within the context of past studies, and
- to determine how frequently NBB rain contains zero bright bands and the roles that echo top height and ice may play in NBB rain intensity and orographic enhancement.

In section 2 we describe the observing system used to gather the data. In section 3 we describe the techniques used to objectively categorize and analyze the data. Section 4 presents the results of our analysis. In section 5 we discuss the results relative to previous studies and provide a brief conclusion in section 6.

2. Observing systems

This study utilized four precipitation-observing sites, two mountain: CZD and Middletown (MDT; Fig. 1; Table 1), and two sites in the Russian River Valley: Santa Rosa (STR; Fig. 1; Table 1) and Hopland (HOP; Fig. 1; Table 1). Additionally, the BBY coastal atmospheric monitoring site was used to observe the landfalling atmospheric forcing for NBB rain. The instrumentation at the precipitation-observing and atmospheric forcing sites and the supplemental numerical weather model

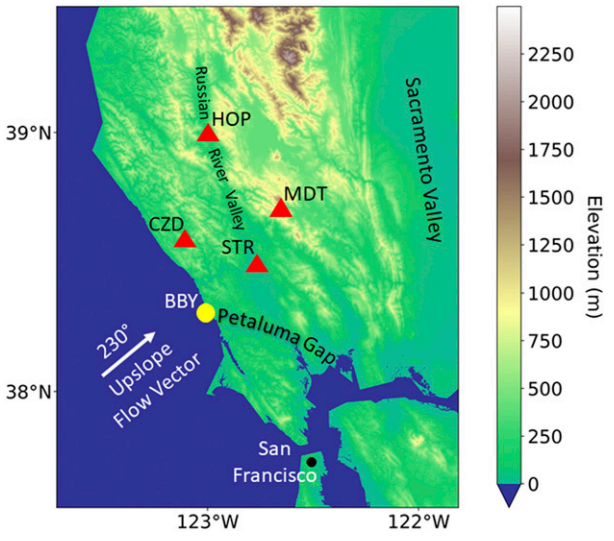

FIG. 1. Study area in the Coastal Mountains of Northern California. Precipitation-observing sites are located at the red triangles. The coastal atmospheric forcing site is located at the yellow circle.

data used in this study are described below and are listed in Table 1 (NOAA/NCEI 2017; NOAA/PSL 2017).

a. Precipitation-observing sites

NBB rain was identified using four vertically pointing, 3-GHz, S-band precipitation profiling radar (S-PROF; Ecklund et al. 1999; White et al. 2000). The S-PROFs provided sampling of the precipitating structure at 60-m range gate resolution and maximum sample height of 8.5 km AGL. Each sample measured the reflectivity and Doppler vertical velocity at a temporal sampling rate of ~1 min. S-PROF data were used to categorize precipitation type, derive echo top heights, and evaluate altitude of hydrometeor growth.

Collocated with the S-PROFs are ground-based, in situ measurements of precipitation. Each site is equipped with a TE525 tipping-bucket rain gauge (heated at MDT) which provided the rain rate data for this study. The rain gauge has a measurement resolution of 0.254 mm (i.e., one tip) resulting in a minimum rain rate of 0.254 mm h^{-1}. The measurement accuracy is ±1% at rain rates ≤ 25.4 mm h^{-1}, encompassing the rain rates commonly observed as NBB rain (White et al. 2003). These gauges were unshielded, which can cause undercatch in windy conditions (Sieck et al. 2007; Kochendorfer et al. 2017), disproportionately affecting higher-altitude gauges (Pollock et al. 2018), and snowfall (Rasmussen et al. 2012; Grossi et al. 2017). No undercatch correction is performed in this study and is thus a potential source of error in the analysis.

In addition to the tipping-bucket rain gauge, CZD and MDT were equipped with a Joss–Waldvogel RD-80 impact disdrometer (Joss and Waldvogel 1967). The disdrometer consists of a 50-cm^2 sampling area that transforms the mechanical momentum of an impacting drop into an electric pulse. The measurable range of drop diameters is 0.3–5-mm spread across 127 size classes distributed roughly exponentially over the diameter range with an accuracy of ±5% of the drop diameter. Note that the momentum impact of drops smaller than 0.3 mm is too weak to be accurately identified by this instrument but likely occur in NBB rain events.

b. Coastal atmospheric monitoring site

To understand the atmospheric forcing behind NBB rain we utilized the BBY coastal atmospheric monitoring site. Wind speed and direction measurements were taken with a 449-MHz wind profiler (White et al. 2013) with ±1 m s^{-1} accuracy. The wind profiler has a height coverage of 195–10 000 m AGL, depending on atmospheric conditions. Two height-resolution modes were operated with 101.4-m vertical resolution in roughly the boundary layer and 202.8-m vertical resolution above the boundary layer. A single wind profile was measured over a period of 30–90 s and was then averaged over a 60-min period using a consensus routine which filters outliers using threshold and acceptance windows (Weber et al. 1993).

BBY has a Radio Acoustic Sounding System (RASS), which measures vertical profiles of acoustic temperature (May et al. 1988).

TABLE 1. Observing stations and instrumentation.

Location	Station ID	Lat (°N)	Lon (°W)	Elev (m)	Instrumentation
Bodega Bay, CA	BBY	38.32	123.07	15	449-MHz wind profiler RASS GPS IWV Rapid Refresh (RAP)[a]
Santa Rosa, CA	STR	38.52	122.80	32	3-GHz precipitation profiler Tipping-bucket rain gauge
Hopland, CA	HOP	39.00	123.09	253	3-GHz precipitation profiler Tipping-bucket rain gauge
Cazadero, CA	CZD	38.61	123.22	478	3-GHz precipitation profiler Tipping-bucket rain gauge Joss impact disdrometer
Middletown, CA	MDT	38.75	122.71	972	3-GHz precipitation profiler Tipping-bucket rain gauge Joss impact disdrometer

[a] RAP numerical weather model used for freezing level heights at this site.

The temperature measurement accuracy of the RASS system is ±1°C root-mean-square error when compared to radiosondes (May et al. 1989; Martner et al. 1993). Vertical and temporal resolution are similar to the 449-MHz wind profiler and also combine 1-min observations into hourly averages that are filtered by the Weber et al. (1993) method. The measurement range is approximately 0.5–2.0 km AGL with lower ranges occurring in high-wind, heavy-rain environments.

Using a global positioning system (GPS) receiver and surface measurements of atmospheric temperature and pressure, the signal delay between satellites and the receiver can be used to estimate the amount of IWV in the atmosphere (Bevis et al. 1992). This technique has since been applied across the globe for research and operational purposes (e.g., Guerova et al. 2003; Mattioli et al. 2007; Neiman et al. 2009; Li and Deng 2013; White et al. 2013). IWV measurements using this method have an accuracy of 0.5 mm when compared to radiosondes and microwave radiometers (Wolfe and Gutman 2000). For this study, GPS IWV measurements were taken every 30 min at BBY and averaged by the hour to match observations from the wind profiler and RASS system.

Since the RASS system can often only measure temperature in the lowest 2 km of the troposphere and radiosondes were not operationally launched on hourly intervals, we supplement the atmospheric monitoring site dataset with freezing level heights from the rapid refresh (RAP) numerical weather prediction model (NOAA/NCEI 2017). Freezing level height is defined as top-down search for the first interpolated altitude where $T = 0$°C at the grid point closest to BBY from the operational RAP 0-h analyses. The RAP 0-h analyses were chosen due to the authors examination of NOAA's S-band radar snow verification tool. Model output from the Global Forecast System (GFS), which is used to initialize and update boundary conditions for the RAP was tested for snow level accuracy and is generally within 300 m of the observed height (White et al. 2010; Neiman et al. 2014). However, these studies looked at forecasted snow levels and we are using 0-h analyses, so we expect errors to be reduced. Note that we do not verify the accuracy of the freezing level height in this paper and this a possible source of error in the analysis.

3. Methodology

Precipitation observed by S-PROFs is objectively categorized by precipitation type using brightband height detection (White et al. 2002) and process partitioning algorithms (White et al. 2003). The algorithms were performed using all precipitation profiles in a half-hour period (~30 profiles) as long as precipitating profiles were detected. If ≥50% of the precipitation profiles identified a bright band, then it is considered BB rain. NBB rain is defined as a 30-min period of rain where <50% of precipitation profiles exhibited a BB. We used 30-min periods to match the temporal resolution of other studies of seasonal precipitation contributions from different microphysics regimes (e.g., White et al. 2015). To trigger these algorithms, the tipping buckets located at S-PROFs must record at least two tips (0.508 mm) within the half-hour period resulting in a minimum rain rate of ~1 mm h^{-1}. If only one tip was recorded in the half-hour period, it is designated as trace precipitation. Additionally, snow was categorized using surface temperature, optical disdrometer, and continuity of brightband time–height series based on the situation and data available at each site (see White et al. 2015). Since convective rain periods often do not produce bright bands because of strong vertical motions and turbulence that mix ice and liquid hydrometeors around the freezing level, these periods were objectively categorized as NBB rain. NBB rain periods were then manually searched to identify convective periods through the same methods and by the same researchers as in previous studies (see White et al. 2003; Neiman et al. 2005). After the algorithms and convective sorting were complete, we result in five precipitation types used in this study: BB rain, NBB rain, snow, convection, and trace. We used the 30-min resolution precipitation type to calculate the seasonal contributions for consistency with other studies (e.g., Neiman et al. 2005; White et al. 2015).

The 30-min precipitation type data are combined into hourly resolution to match the temporal resolution of atmospheric forcing site data. Beyond this point we only evaluate NBB rain hours. To identify the hours containing only NBB rain, we require that the hour must contain at least one 30-min period categorized as NBB rain and if only one was observed as NBB rain, the other 30-min period may only be categorized as trace or no precipitation. This process isolated periods when NBB rain was the dominant precipitation type. The echo top height for each hour is defined as the median height with signal-to-noise ratio (SNR) of −16 dB in the range-corrected noise profile. The echo top from S-PROF radar will differ from higher-frequency radars and lidars that may be more sensitive to the smaller particles and weaker scattering regions near some cloud tops (e.g., cirrus).

Next, we created subsets of NBB rain based on the brightband percentage in the hour period. Three categories are defined: when BB < 50% (hereafter NBB_{50}), BB < 20% (hereafter NBB_{20}), and BB = 0% (hereafter NBB_0). The 20% threshold was chosen to eliminate when BB rain comprises a substantial portion of the precipitation time. The 0% threshold is the closest to pure warm rain that can be identified by the radar, but importantly does not mean that ice-phase processes were not occurring.

Additional quality control of NBB rain hours was necessary to remove data that can affect the accuracy of hourly rain rate and echo top height measurements. For example, occasionally precipitation from an upper-level cloud, separated from the shallow NBB rain profiles by a dry layer, can extend downward and effectively seed the NBB feeder cloud below. These occurrences are subjectively removed by identifying profiles of continuous SNR exceeding 52 dB, the threshold to eliminate noise from precipitation (White et al. 2002), that extend from upper-level clouds (>5 km MSL echo tops) into areas of established NBB rain. Additionally, precipitation may only occur for a short portion of the hour-long period. These NBB rain hours can contribute minimal precipitation amounts despite having relatively high echo tops and skew correlations between rain rate and echo top height. Thus, we removed NBB rain hours that had fewer than 66% precipitating profiles. This step

disproportionately affected the two valley sites, STR and HOP, due to subhourly discontinuities in NBB rain often observed in the valleys. It appears that as orographically forced clouds move over the Russian River Valley they weaken to the point where precipitation profiles display discontinuities (in time). The resulting NBB rain dataset consists of 15 h at STR, 33 h at HOP, 82 h at CZD, and 306 h at MDT. Given the much smaller sample sizes at STR and HOP, we did not analyze atmospheric forcing at these sites.

To understand atmospheric forcing of NBB rain, lower tropospheric profiles of upslope wind and stability for each hour were used. Upslope wind speed was calculated as the absolute wind speed perpendicular to the range. As in Neiman et al. (2002, 2009), we used 230° as the upslope wind direction for CZD and consider ±90° of 230° as our upslope window. The orientation of the MDT range is similar to CZD, and correlations for other upslope wind directions were tested and 230° had the strongest correlations with rain rate and was used for both sites. Upslope wind speed profiles were calculated across the 150–3950 m MSL height range and were subject to a 300-m averaging window as in Neiman et al. (2002, 2009). All correlations in this study were calculated from linear least squares regressions with statistical significance from the Wald test.

To evaluate the stability upwind of the mountains, the dry Brunt–Väisälä frequency squared was calculated using

$$N^2 = \frac{g}{\theta_v}\frac{d\theta_v}{dz}, \tag{1}$$

where g is gravity, θ_v is the mean virtual potential temperature in the layer, and $d\theta_v/dz$ is the change in potential temperature over that layer. Dry air stability was used instead of moist because observations on an hourly temporal resolution were not available to calculate such metric. Measurements of acoustic temperature were provided directly from the RASS system and were converted to virtual temperature using collocated surface observations. Then a known surface altitude, observed station pressure, and observation altitude were used with the hypsometric equation to calculate θ_v. Stability and rain rate were only compared at the MDT site because of the large sample size. Stability was calculated for the 150–950 m MSL layer, which encompasses the lowest range gate from RASS to the altitude of MDT. Additionally, the bulk Froude Number squared was calculated using stability and upslope wind speed in the 150–950 m MSL layer following Eq. (6) from Hughes et al. (2009).

To provide insight on the microphysical processes occurring, disdrometer measurements of drop-size distribution (DSD) were used. Impact disdrometers experience a phenomenon called "dead time" where the impact from a drop can cause ringing of the observing cone not allowing for the measurement of subsequent drops for a short time period. To account for the dead time loss, we used the corrected channel counts calculated using Eq. (2) from Sheppard and Joe (1994). This technique uses the observed frequency of drops in each channel (bin) to estimate the additional drops that fell during this dead time. DSDs are not accurate when winds exceed 10 m s^{-1} at the surface due to small drops not impacting the disdrometer. Therefore, if the surface wind speed exceeds 10 m s^{-1} for more than 15 mins h^{-1}, DSDs were not used for analysis.

TABLE 2. Total wet-season (November–March) precipitation and precipitation time.

	Precipitation (mm)		Precipitating hours	
Station ID	2016	2017	2016	2017
STR	738	1154	386	501
HOP	827	1186	445	554
CZD	1382	1344	413.5	435
MDT	1763	2802	578	703.5

A preliminary analysis of a 1-day sample of 2-min resolution disdrometer data from MDT were used to evaluate DSD characteristics of 12 h of NBB rain and 10.2 h of BB rain. It was found that the number of raindrops that exceed drizzle size (>0.5-mm diameter; hereafter large drops) was statistically significantly correlated at the 95% confidence interval with NBB rain rate with an r^2 value of 0.81, $p < 0.05$ ($r^2 = 0.07$, $p > 0.05$ for BB rain). The correlation between total drops of all sizes and NBB rain rate was weaker than the large drops alone ($r^2 = 0.50$, $p < 0.05$). These results suggest that NBB rain rates are highly dependent on the ability of the cloud to generate raindrops that exceed drizzle size. Despite the short duration of the 1-day sample used in the analysis, the results were significant enough to develop a metric to quantify the ability of NBB rain clouds to convert small drops (i.e., drizzle; 0.3–0.5-mm diameter) to large drops, called growth efficiency (GE),

$$\mathrm{GE} = \frac{N_{>0.5\mathrm{mm}}}{N}, \tag{2}$$

where $N_{>0.5\mathrm{mm}}$ is the number of large drops, and N is the total number of drops measured by the disdrometer. Therefore, a GE of 0.25 equates to 75% of the drops being drizzle size and 25% of the drops being larger than drizzle. GE is a useful metric because it is not sensitive to the total number of drops, and thus can provide better insight on microphysics than large drop count alone. In this paper GE is divided into four categories: when $0 \le \mathrm{GE} < 0.25$ (hereafter $\mathrm{GE}_{0\text{–}0.25}$ or low-GE), $0.25 \le \mathrm{GE} < 0.5$ (hereafter $\mathrm{GE}_{0.25\text{–}0.5}$), $0.5 \le \mathrm{GE} < 0.75$ (hereafter $\mathrm{GE}_{0.5\text{–}0.75}$), and $0.75 \le \mathrm{GE} \le 1$ (hereafter $\mathrm{GE}_{0.75\text{–}1}$ or high-GE).

4. Results

a. Microphysical regimes

First, we discuss the role of microphysical regimes on wet-season precipitation from the process partitioning algorithm. Total precipitation and precipitating hours for the four precipitation-observing sites over both wet seasons are shown in Table 2 and the percentages of seasonal precipitation amount and precipitating hours for each precipitation type are broken down in Fig. 2. Two-season average NBB_{50} rain was 214 mm (120 h) at STR, 153 mm (107 h) at HOP, 387 mm (143 h) at CZD, and 761 mm (267 h) at MDT. Despite HOP

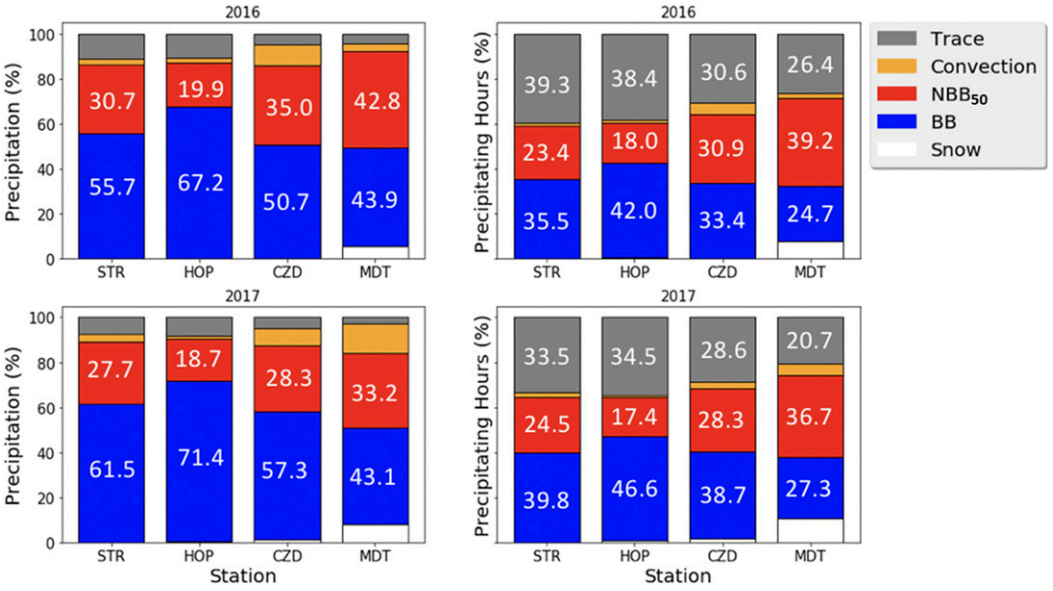

FIG. 2. Percentage of wet season (November–March) precipitation and precipitating hours. The 2015/16 wet season and 2016/17 wet season are labeled by their water years, or 2016 and 2017, respectively.

observing more total precipitation than STR in both seasons, STR observed a much larger percentage of NBB_{50} rain (27.7%–30.7%) than HOP (18.7%–19.9%) and 61 mm yr^{-1} more in the two-season average (Fig. 2). In fact, percentage contributions of NBB_{50} rain at STR are much more akin to the nearby mountain site of CZD (28.3%–35%). Alternatively, HOP received ~10% larger contribution from BB rain than STR, explaining the higher total precipitation per season observed at HOP (Table 2).

NBB_{50} rain was more common and contributed more to seasonal precipitation amount at mountain sites with a substantial increase from CZD to MDT. CZD observed ~81% more and MDT observed ~256% more seasonal NBB_{50} rain compared to STR. However, CZD observed only 23 more NBB_{50} rain hours than STR while MDT observed 147 more NBB_{50} rain hours. However, the lower-elevation sites observed a much larger seasonal contribution from trace precipitation. In 2015/16, STR and HOP observed ~11% of total precipitation from trace, while CZD and MDT observed <5% (Fig. 2). These precipitation amount data are reflected in the precipitating hours, where trace precipitation hours accounted for more than a third of all precipitating hours at the two valley sites. The contributions from trace precipitation appear to diminish with altitude, as CZD observed 5%–8% fewer trace precipitating hours than the valley sites and MDT observed 4%–8% less than CZD (Fig. 2). This trend suggests that NBB rain may have been falling across the entire region but was only meeting the ~1 mm h^{-1} threshold to trigger process partitioning at MDT, while only trace precipitation was being recorded at other sites. During times when MDT observed NBB rain and CZD did not (354 h), CZD observed trace 25% of the time and no precipitation 64% of the time. Similarly, when CZD observed NBB rain but STR did not (177 h), STR observed trace 37% of the time and no precipitation 36% of the time. Thus, when NBB rain is falling over the higher elevations of the Northern Coast Ranges it is likely falling across the region, but at intensities too low to trigger the process partitioning algorithm (i.e., trace) or a single tip from the tipping-bucket rain gauge (i.e., no precipitation) at lower elevation sites.

b. *The roles of echo top height and wind*

Linear regressions of NBB_{20} rain rate and echo top height were investigated to understand the role of higher precipitating clouds on rain intensity. We find the strongest correlation between echo top height and rain rate at HOP ($r = 0.77$, $p < 0.05$), and a linear regression that indicates higher echo tops than other sites are necessary to produce rain rates of similar magnitude (Fig. 3). The linear regression at HOP suggests a 3 km MSL echo top would produce a rain rate of 1.58 mm h^{-1}. STR and CZD exhibit similar echo top dependencies on NBB rain rates; STR ($r = 0.65$, $p > 0.05$); CZD ($r = 0.73$, $p < 0.05$). Therefore, an echo top of 3 km MSL would produce a rain rate of 3.22 mm h^{-1} at STR and 3.57 mm h^{-1} at CZD. However, the sample size was too small at STR to produce a statistically significant correlation at the 95% confidence interval. MDT was the most efficient at producing NBB rain at lower echo tops as evidenced by the shallowest regression line ($r = 0.65$, $p < 0.05$). Based on the linear regression, a 3 km MSL echo top at MDT would produce an NBB rain rate of 5.97 mm h^{-1} (Fig. 3). From these linear regressions we find that echo top height can explain 42%–59% of the variance in NBB_{20} rain rates depending on location.

To understand the atmospheric forcing that drives echo top heights and rain rates, we created correlation coefficient vertical profiles in the same manner as Neiman et al. (2002). The correlation coefficient profile of BBY upslope wind and CZD NBB_{20} rain rate (Fig. 4) shows a similar pattern to Neiman et al. (2002, 2009). The correlation coefficient is maximized

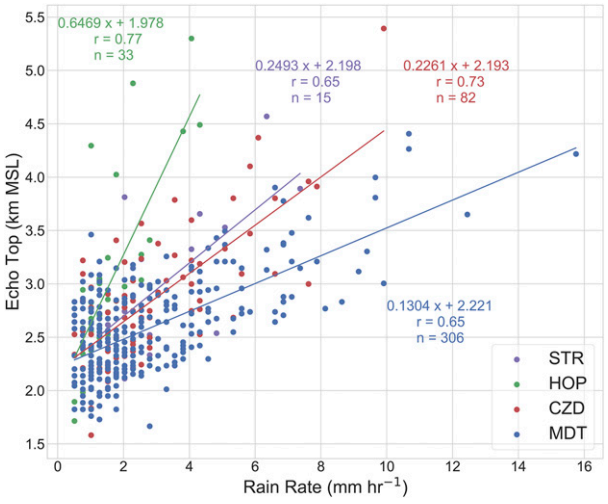

FIG. 3. NBB_{20} rain rate by echo top height. Precipitation must be occurring in a minimum of 66% of the S-PROF profiles.

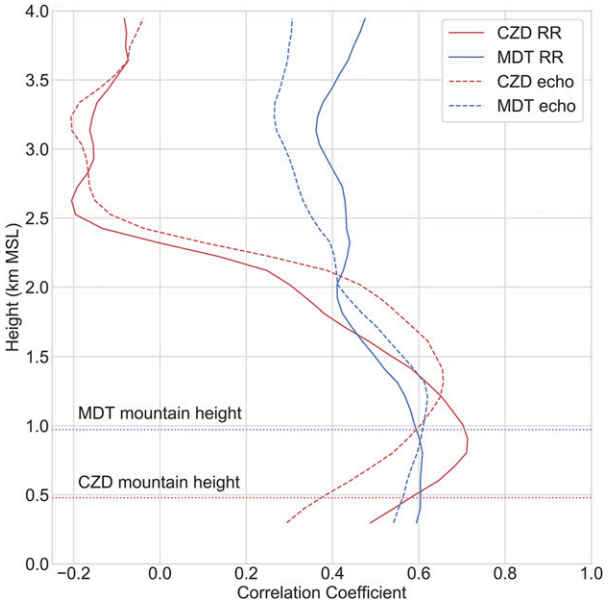

FIG. 4. Correlation coefficient profiles between upslope wind speed and NBB_{20} rain rate, NBB_{20} echo top height for CZD and MDT. Data must be available from the BBY wind profiler up to 4 km MSL, resulting in $n = 43$ h for CZD and $n = 155$ h for MDT.

above the altitude of CZD in the 750–1050 m MSL layer-averaged upslope wind ($r = 0.71, p < 0.05$), similar to the 950 m MSL height observed by Neiman et al. (2002). We observed a higher correlation coefficient than their study ($r = 0.64$), which is possibly due to our datasets focus on orographically forced NBB_{20} rain, while their study incorporated all rain types. Alternatively, the maximum correlation coefficient for MDT rain rate occurs below MDT mountain height in the 650–950 m MSL layer ($r = 0.61, p < 0.05$). Neiman et al. (2002) concluded that the reason the CZD correlation coefficient was maximized above mountain height was due to blocked flow that can occur offshore of the Northern Coast Ranges. Given the correlation coefficient profile for MDT, it appears that low-level blocked flow has a lesser impact on NBB rain rates at this site. One possible physical reasoning is that blocked flow along the coast is often necessary to produce NBB rain at CZD by forcing unblocked moist air to rise over it. However, MDT observed much more NBB rain and is located on a taller range that may better force NBB rain without the aid of blocked flow due to a larger vertical displacement of impinging air.

The correlation coefficient profiles between BBY upslope wind speed and CZD and MDT echo top heights are similar to the rain rate correlation profiles, with maxima shifted 400 m higher (Fig. 4). The maximum correlation coefficient at CZD is in the 1150–1450 m MSL layer ($r = 0.66, p < 0.05$), and at MDT in the 1050–1350 m MSL layer ($r = 0.62$, $p < 0.05$). These correlations indicate that 38%–44% of the variance in echo top height can be explained by upslope wind speed. While other factors such as stability, moisture availability and other lifting mechanisms that can affect echo top height are not considered, the correlation coefficients suggest that upslope wind speed is an important forcing mechanism for echo top height in NBB_{20} rain. It is unclear if the physical reason for this correlation is due to deeper clouds in strong wind conditions or from more efficient growth of hydrometeors. We found upslope wind speed to be highly correlated to the dry air Froude number ($r = 0.75$, $p < 0.05$), where weaker winds often resulted in blocked flow (Froude number < 1). The blocked flow, or terrain trapped airflows, common in this geographical region can affect the streamlines of airflow over the mountains leading to different cloud structures (Neiman et al. 2002; Valenzuela and Kingsmill 2018; Ryoo et al. 2020). Unblocked flows translate into faster vertical velocities than blocked flows with equivalent impinging horizontal wind speeds due to the steeper angle of ascent. Faster upslope wind speeds also translate into faster vertical velocities, leading to higher supersaturation in clouds and may result in more efficient growth of precipitation and thus higher echo tops (Korolev and Mazin 2003). Note that multiplying IWV by upslope wind speed to produce bulk upslope IWV flux as in Neiman et al. (2009) and Kingsmill et al. (2016) did not provide a statistically significant improvement in maximum correlation coefficients with NBB rain rate or echo top height at either CZD or MDT. In fact, the correlation coefficients with bulk upslope IWV flux decreased in all relationships besides MDT echo top height ($r = 0.63$).

To better understand why MDT observed much more NBB rain than CZD, we investigated the roles of wind direction and speed and their relationships with rain rate (Fig. 5). As expected, the heaviest rain rates occur when the wind direction within the upslope wind layer with the strongest correlation with rain rate (650–950 m MSL) is directed perpendicular to the ranges (230°) and when wind speeds are stronger (i.e., stronger upslope wind speed). However, most of the NBB_{20} rain at CZD occurs with wind directions counterclockwise of the upslope angle (230°), with many fewer NBB_{20} rain hours under more westerly winds. Alternatively, MDT observes NBB_{20} rain with westerly winds (~270°), though the intensity

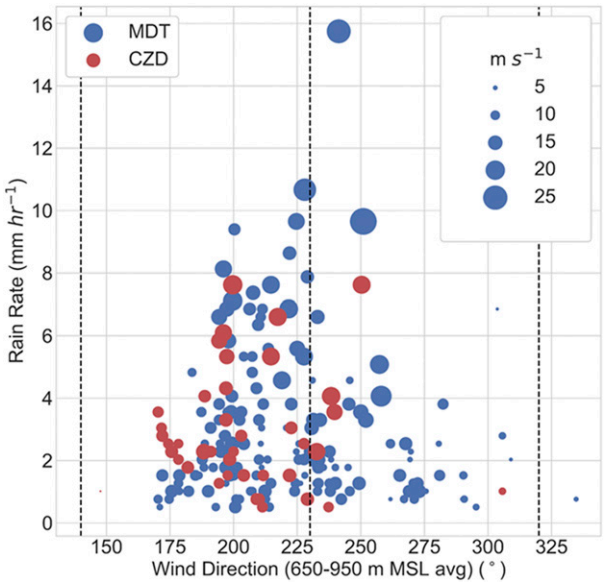

FIG. 5. Hourly NBB_{20} rain rate and wind direction in the layer with the strongest correlation between upslope wind speed and rain rate (650–950 m MSL). The 650–950 m MSL layer is used because the upslope wind speed in this layer explains the most combined variance in CZD and MDT rain rates (Fig. 4). The upslope window is defined as ±90° of the upslope angle of 230°.

tends to be less than 4 mm h^{-1}. These results suggest that weaker wind speeds (<15 m s^{-1}) clockwise of 260° commonly produce NBB_{20} rain at MDT, but rarely at CZD, perhaps due to the higher-altitude terrain around MDT. These weaker westerly winds may occur behind cold fronts in landfalling storms; however, they would be accompanied by a descending freezing level which would increase the likelihood of ice-phase microphysics (Kingsmill et al. 2006).

c. *The role of ice*

The distributions of NBB rain rates show frequency of NBB_{50}, NBB_{20}, and NBB_0 rain rates at each site to provide insight into the importance of ice microphysics (Fig. 6). The maximum NBB rain rate (all categories) was lowest at HOP (6 mm h^{-1}), followed by STR (13 mm h^{-1}), CZD (16 mm h^{-1}), and MDT (22 mm h^{-1}). The decrease of the rain rate frequency bars (on a logarithmic y scale) is the steepest for HOP, which received less seasonal NBB_{50} rain (Fig. 2) and lighter average NBB_{50} rain rates (Fig. 3). The decrease in rain rate frequency with increasing intensity is less sharp as elevation increases, demonstrating how light NBB rain rates (0–2 mm h^{-1}) are common at all sites and NBB categories, but increasingly heavy rain rates become increasingly more common as elevation increases (Fig. 6). Additionally, we find that 81% of NBB_{50} hours were retained at the BB_{20} threshold, and 38% of NBB_{50} hours were retained at the NBB_0 threshold in the four-site average. However, sites were affected differently based on location. HOP and CZD observed similar retention in NBB_{20} of 73% at HOP and 77% at CZD and NBB_0 of 32% at HOP and CZD. STR and MDT observed higher retention in NBB_{20} of 84% at STR and 85% at MDT and in NBB_0 of 46% at STR and 40% at MDT. These data suggest that bright bands are more common in NBB rain at the HOP and CZD sites than the STR and MDT sites. Perhaps the most notable difference in the NBB categories is the effect on the heaviest rain rates. We find that valley site NBB_0 rain rates were <5 mm h^{-1}, and mountain site NBB_0 rain rates were <10 mm h^{-1} (Fig. 6). However, NBB_0 rain rates rarely exceeded 3 mm h^{-1} in the valleys and 7 mm h^{-1} in the mountains in our dataset. As noted by White et al. (2003), local forecasters commonly use ≥12 mm h^{-1} as a threshold for issuing flood guidance. All NBB rain rates that exceeded that threshold were in the NBB_{20} and NBB_{50} categories, suggesting that ice microphysics is necessary to achieve flood-threatening rain rates from NBB rain alone whereas lighter NBB rain rates may add to flood risk only in events with heavier rainfall from other precipitation types (e.g., BB rain).

Ice microphysics also affected the orographic enhancement of NBB rain on the hourly and seasonal time scales (Fig. 7). When all sites were observing NBB_{50} rain, there was a clear orographic enhancement between STR, CZD, and MDT (Fig. 7a). With STR as a reference rain rate, CZD received 1.71 times higher NBB_{50} rain rate and MDT received 2.54 times higher NBB_{50} rain rate, approximately double the orographic enhancement of CZD. Conversely, the HOP site received 0.65 times the NBB_{50} rain rate of STR. The impact of ice on orographic enhancement was different over seasonal scales. Total NBB_0 rainfall at HOP was only 0.4 of the total at STR with increasing fractions with increasing frequencies of bright bands in the NBB_{20} and NBB_{50} categories (Fig. 7b). Similarly, total rainfall at CZD with respect to STR increased from 1.08 to 1.77 and at MDT from 3.09 to 3.49 as brightband frequencies increased. These trends suggest that when ice is more commonly present in NBB rain clouds, the orographic enhancement increases. However, we note that Kingsmill et al. (2016) found that orographic enhancements at CZD with respect to BBY were larger in NBB rain compared to BB rain. It is important to understand that the NBB_{50} orographic enhancement factors are larger in the seasonal time scale (Fig. 7b) compared to the average NBB_{50} rain rate (Fig. 7a) because the seasonal data includes additional hours when NBB_{50} rain is falling at CZD and MDT and not at STR. The larger increase at MDT (from 2.54 to 3.49) compared to CZD (from 1.71 to 1.77) alludes to the much higher frequency of NBB_{50} rain at MDT than CZD with respect to STR, much of which is due to the ability of MDT to produce NBB rain at lower echo top heights than CZD.

Despite strong correlation, we find that echo top height can only explain 42% of the variance in NBB_{20} rain rates at MDT (Fig. 3). Certain echo top heights show larger variance in rain rate than others (Fig. 8). For example, an echo top of 3 km MSL at MDT can produce NBB_{20} rain rates anywhere from 1 to 10 mm h^{-1}. We find that when the average drop count is not too low (≥500 drops min^{-1}), GE may explain a lot of variance not explained by echo top height ($r^2 = 0.35$, $p < 0.05$; Fig. 8). Each category of GE is plotted in Fig. 9 to show their inherent differences in DSDs. Low-GE ($GE_{0–0.25}$) is comprised mainly of drizzle with few drops exceeding 1 mm diameter and no drops larger than 2 mm. The three higher GE categories have raindrops that exceed 3 mm in diameter and progressively fewer

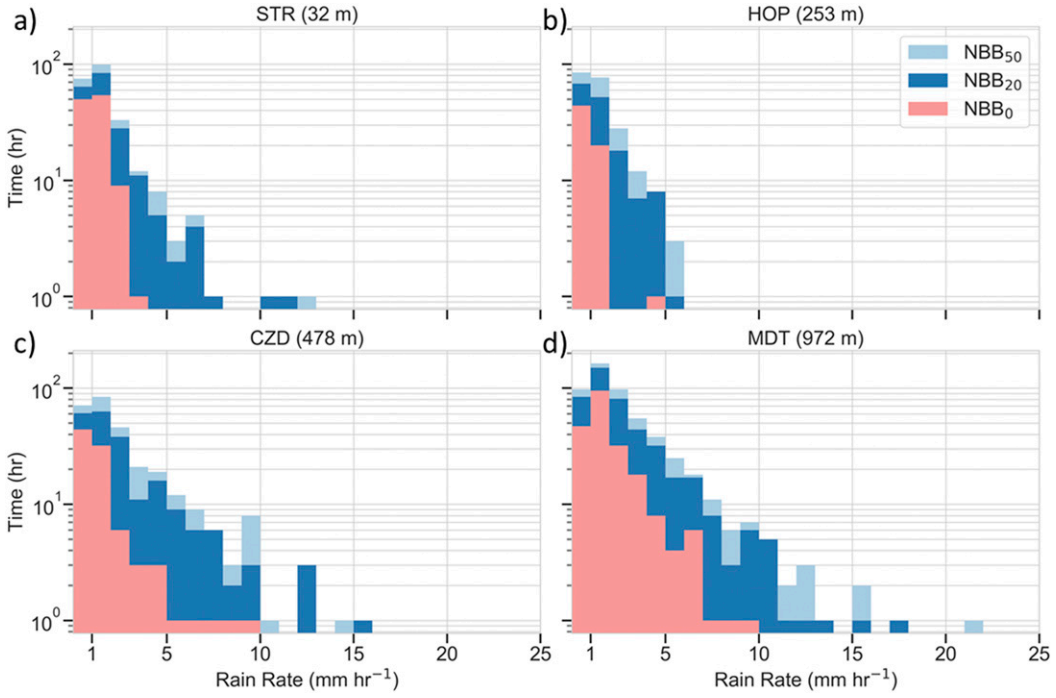

FIG. 6. Frequency of hourly rain rate in the NBB regime in 2016 and 2017. NBB_{50} depicts all hours classified as NBB rain, NBB_{20} contains hours with less than 20% bright bands, and NBB_0 contains hours with no bright bands. The *y* axis is logarithmic.

drizzle sized drops as GE increases. The main difference between $GE_{0.25–0.5}$, $GE_{0.5–0.75}$, and $GE_{0.75–1}$ occurs in the 1–2-mm diameter range where higher GEs are associated with substantially more drops in that size range. The differences in the drop counts beyond 2 mm appear large because of the logarithmic axis, but only account for a few drops and have a lesser impact on rain rate compared to the differences in 1–2-mm drops. The average NBB_{20} rain rates increase logically from

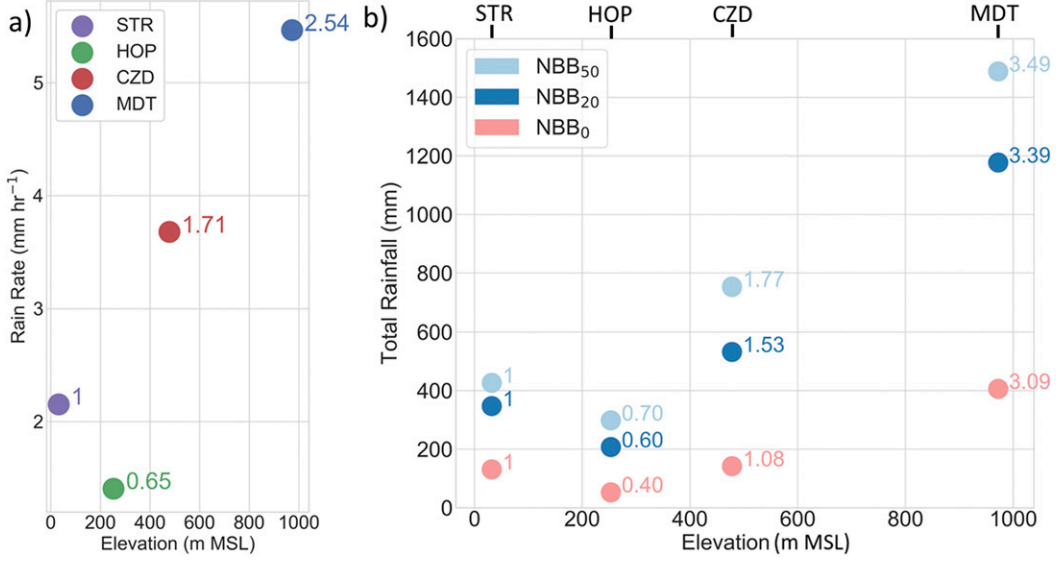

FIG. 7. (a) Average NBB_{50} rain rate when all four sites were recording NBB_{50} rain over the two-season period ($N = 40$ h). Numbers next to data points show orographic enhancement factor with respect to the STR site rain rate. (b) Total two-season rainfall from NBB_{50}, NBB_{20}, and NBB_0 rain at each site. Numbers next to data points show season-long orographic enhancement factor with respect to the STR site total rainfall.

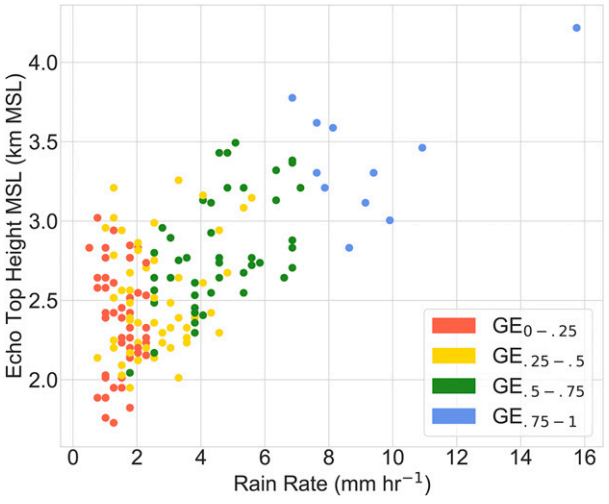

FIG. 8. NBB$_{20}$ rain rate at MDT by echo top height and growth efficiency (GE) at all hours with an average ≥ 500 drops min^{-1}. The four GE categories are as follows: when $0 \le GE < 0.25$ (GE$_{0–0.25}$ or low-GE), $0.25 \le GE < 0.5$ (GE$_{0.25–0.5}$), $0.5 \le GE < 0.75$ (GE$_{0.5–0.75}$), and $0.75 \le GE \le 1$ (GE$_{0.75–1}$ or high-GE). Mean rain rates were 1.32 mm h^{-1} for GE$_{0–0.25}$, 2.09 mm h^{-1} for GE$_{0.25–0.5}$, 4.06 mm h^{-1} for GE$_{0.5–0.75}$, and 5.94 mm h^{-1} for GE$_{0.75–1}$.

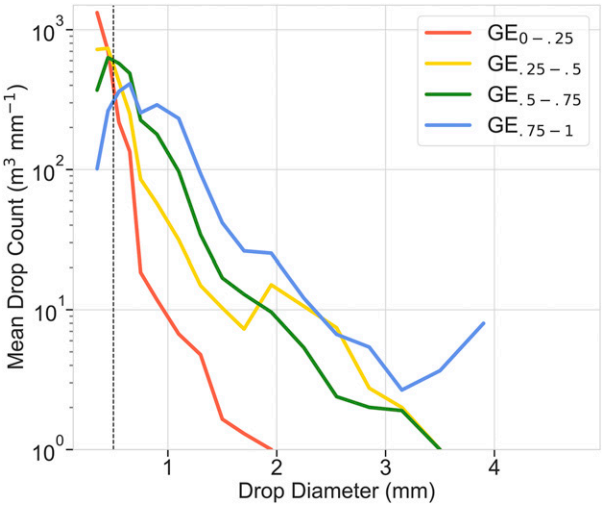

FIG. 9. NBB$_{20}$ mean drop count at each drop size per 2-min sample of all NBB$_{20}$ hours by GE category. The *y* axis is on a logarithmic scale. The vertical black dashed line shows the cutoff of small drops (drizzle) and large drops (raindrops). Mean NBB$_{20}$ rain rate for each GE category are shown in the Fig. 8 caption.

low-GE to high-GE as suggested by Fig. 8 (see Fig. 8 caption). Higher GE may occur from higher echo top heights and greater chance for hydrometeors to grow via collision–coalescence, or through mixed-phase processes that rapidly grow hydrometeors to larger size and increase the efficiency of coalescence.

Echo top height and the difference between echo top height and freezing level height show that both higher echo top heights and mixed-phase processes may lead to higher GE (Fig. 10). Median echo top heights ascend along with rising GE; however, the differences are less for GE$_{0–0.25}$ and GE$_{0.25–0.5}$ (Fig. 10a). The notches around the median in each box plot show the 95% confidence interval of the median echo top height. The GE$_{0–0.25}$ and GE$_{0.25–0.5}$ medians are not statistically significantly different from each other, but the GE$_{0.5–0.75}$ and GE$_{0.75–1}$ medians are statistically significantly different from the lower GE medians and from each other. The difference between the echo top height and freezing level height shows the increasingly likelihood that ice may lead to higher GE (Fig. 10b). The interquartile range of low-GE (GE$_{0–0.25}$) is completely negative, meaning that more than 75% of the echo top heights are beneath the freezing level and only the warm rain process would occur. Further, the distribution of GE$_{0–0.25}$ does not extend more than 500 m above the freezing level height. The differences in medians are all statistically significant at the 95% confidence interval except for GE$_{0.5–0.75}$ and GE$_{0.75–1}$. The entire distribution of high-GE (GE$_{0.75–1}$) echo top heights are above the freezing level (Fig. 10b). Therefore, these high-GE hours cannot be assumed as pure warm rain and are the most likely to contain ice. However, just because the echo top extends above the freezing level does not necessarily mean that mixed-phase processes are occurring. We investigate this hypothesis further by looking at the subset of data with echo tops between 2.5 and 3 km MSL because it contains a wide range of rain rates while consisting of a large sample size ($n = 58$) within a narrow echo top height range (Fig. 8).

Using normalized contoured frequency by altitude diagrams (CFADs; Yuter and Houze 1995) of the high- and low-GE NBB$_{20}$ subsets with echo tops between 2.5 and 3 km MSL, we find that mixed-phase growth is suggested in high-GE rain (Fig. 11). Little increase in pseudoreflectivity with decreasing height is observed above the 2.8 km MSL mean freezing level height for low-GE (Fig. 11a), but substantial increases in pseudoreflectivity are observed above the 2.2 km MSL mean freezing level height for high-GE (Fig. 11b). The high-GE median increases from 6 dB at 2.9 km MSL to 17 dB at 2.2 km MSL (Fig. 11b). Conversely, pseudoreflectivity increases little between the minimum of 2 dB at 2.65 km MSL and 8 dB at 2 km MSL and the largest increase occurs in lowest kilometer to a median of 19 dB in low-GE rain (Fig. 11a). High-GE rain is most frequently associated with pseudoreflectivity of 30 dB near the surface, while the low-GE rain is most frequently associated with pseudoreflectivity of 15 dB near the surface. The difference in the normalized CFADs shown in Fig. 12 highlight the different growth regions of high- and low-GE. The median difference is the lowest (2 dB) at 2.9 km MSL, and rapidly increases to 17 dB at 2.2 km MSL, approximately equal to the pseudoreflectivity of high-GE alone, suggesting that high-GE raindrops are large at this altitude while low-GE raindrops remain small. The difference increases down to 1.5 km MSL where a decrease in the high-GE median and continued increase in low-GE median result in more rapid growth in the low-GE environment and a decrease in the median difference. Overall, mixed-phase hydrometeor growth suggested by the abrupt increase in pseudoreflectivity above the freezing level in high-GE leads to more efficient growth both above and below the freezing level down to the lowest

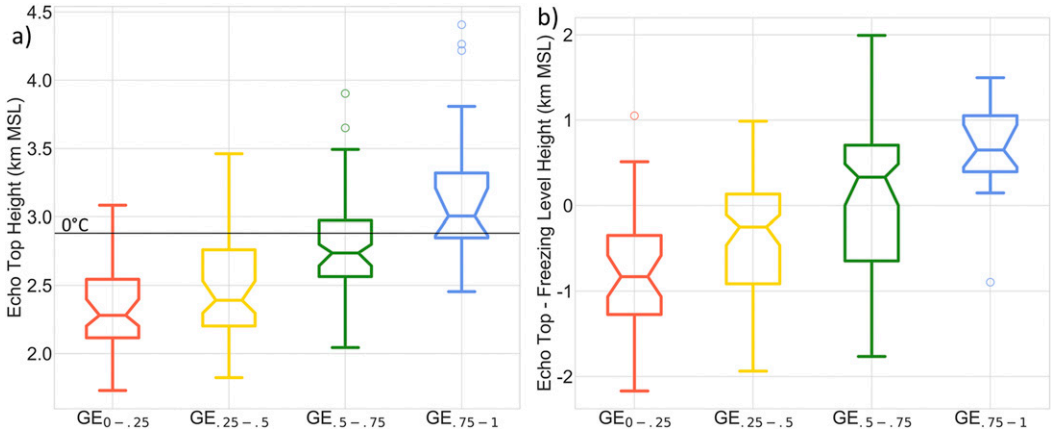

FIG. 10. (a) Echo top height distributions for each GE category. Mean freezing level height across all samples is shown by black line. (b) Difference between echo top height and freezing level height for each GE category. Notches in boxplots shown the 10 000 bootstrap 95% confidence interval around the median (center horizontal line). Where notches do not overlap with another box's notches indicates a statistically significant difference in the medians.

500 m above the surface. Additionally, the difference shows higher frequencies from −10 to 10 dB pseudoreflectivity in high-GE compared to low-GE, which suggests that the high-GE NBB_{20} rain intensity fluctuates and the low-GE NBB_{20} rain is more consistent (Figs. 11 and 12).

d. *Other potential factors*

Since we did not have in situ measurements in the clouds to confirm the presence of ice in high-GE NBB_{20} rain, we must consider other potential factors that can impact rain rate (Fig. 13). We find that in the 2.5–3 km MSL median echo top range, the echo top height accounts for <1% of the variance in NBB rain rates at MDT, while GE accounts for 35% of the variance (Fig. 13a). GE may set an apparent upper limit on NBB_{20} rain rates based on the observations in this study (black line in Fig. 13a). For example, rain rates $\geq 3\ mm\ h^{-1}$ occurred with GE ≥ 0.2 and rain rates $\geq 6\ mm\ h^{-1}$ occurred with GE ≥ 0.5 at MDT. The number of drops is important for rain rate

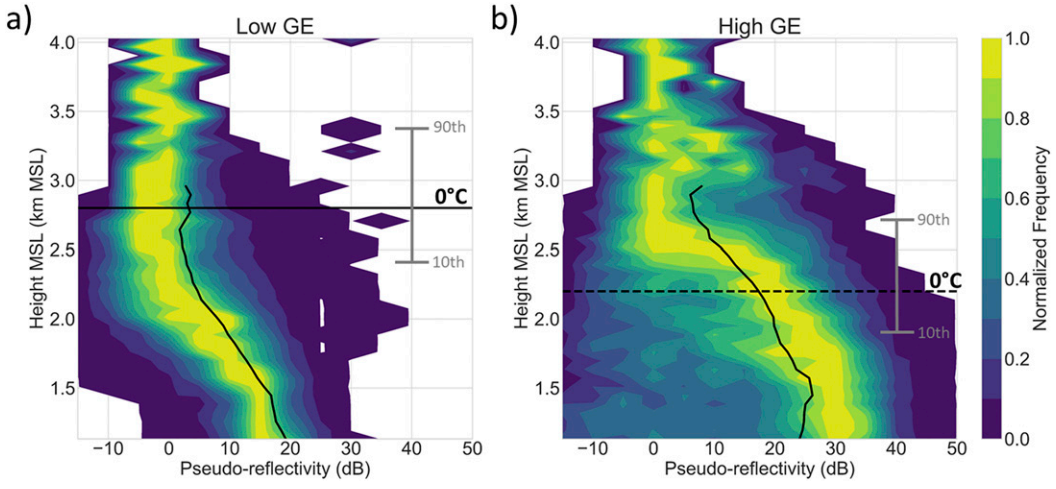

FIG. 11. CFADs of NBB_{20} pseudoreflectivity profiles with median echo top heights of 2.5–3 km MSL at MDT for (a) $GE_{0–0.25}$ and (b) $GE_{0.75–1}$. CFADs are normalized by the maximum frequency of occurrence at each height where 1 represents the maximum. CFADs were binned at 5-dB intervals to reduce noise. The high-GE subset consists of 8 h and the low-GE subset consists of 11 h with ~60 precipitation profiles per hour. Black lines indicated the median pseudoreflectivity at heights where the sample exceeds 100 counts. We refer to reflectivity as pseudoreflectivity since it is based on a calibration from White et al. (2000) and assumes all scattering is from cloud and precipitation rather than clear air. CFADs extend up to 4 km MSL to capture the entire precipitating profile due to variance in echo top height that can occur with a median of 3 km. Average freezing level height is shown by the horizontal solid and dashed black lines labeled 0°C. The 10th and 90th percentiles of freezing level heights are shown within the gray ranges.

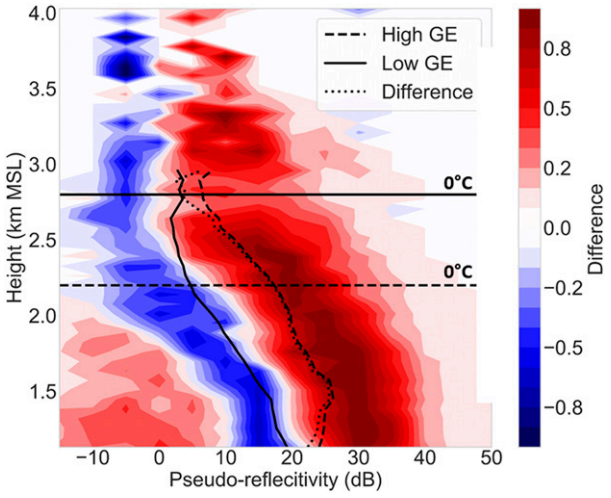

FIG. 12. The difference between the normalized high-GE CFAD and low-GE CFAD from Fig. 11. Difference is shown as high-GE − low-GE. The difference median line is calculated by linearizing the median pseudoreflectivity, subtracting low-GE from high-GE, and converting back to logarithmic. Average freezing level height is shown by the 0°C black lines.

regardless of GE as evidenced by smaller points in Fig. 13a and by the relationship between large drops and rain rate (Fig. 13b). The strong correlation between the number of large drops and NBB_{20} rain rate ($r^2 = 0.72$) using 53 hour-long samples provides further evidence for the importance of GE for NBB rain beyond the preliminary analysis presented in section 3 (Fig. 13b). We also find that upslope wind speed has a statistically significant correlation with NBB_{20} rain rate in this subset (Fig. 13c). This suggests that in addition to a main forcing of echo top height, the upslope wind speed which is redirected vertically over terrain may lead to higher supersaturation and impact the rain rate. IWV did not have a statistically significant relationship with rain rate, but rather with GE, showing that higher GE occurs with lower IWV (Fig. 13d). This relationship may be due to the intrinsic relationship between saturated air temperature and IWV. During saturated conditions, warmer temperatures will have higher IWV, which is shown by the relationship between IWV and freezing level height (Fig. 13e), and by the strong correlation ($r = 0.89$) between IWV and brightband height (Fig. 9c in Neiman et al. 2009). Since higher IWV is associated with higher freezing level heights, it would decrease the impact of mixed-phase processes that are important for heavy NBB rain rates. This relationship may suggest why incorporating IWV into our analysis (Fig. 4) does not improve the correlation and may explain some questions posed by Kingsmill et al. (2016) about the role of IWV. This analysis provides empirical evidence supporting the idealized modeling conclusion of Kirshbaum and Smith (2008) that orographic rain is more efficient with mixed-phase process than warm rain processes despite lower moisture availability (lower IWV) in mixed-phase environments.

It was also possible that NBB_{20} rain rates resulting in high-GE were affected by embedded convection not removed by the manual scanning of precipitation profiles. However, dry stability is greater in higher GE rain hours, which suggests a lower likelihood of embedded convection (Fig. 13f). We cannot rule out embedded convection from moist instability without proper analysis, which is not offered by the dataset herein. To that end, Kirshbaum and Smith (2008) demonstrated that embedded convection primarily redistributes moisture vertically rather than increasing precipitation rates at the surface. The higher dry-stability conditions occurred with lower freezing level heights (Fig. 13g), further suggesting the importance of mixed-phase processes in generating high-GE rain. GE tends to be higher when the echo top extends farther above freezing level height (Fig. 13h) and with more frequent bright bands (Fig. 13i). However, mixed-phase processes can occur without any observing radar bright bands.

5. Discussion

The percentages of NBB_{50} rain observed in this study were normal with respect to the results shown in White et al. (2015). NBB_{50} rain comprised 28.3%–35% of the seasonal precipitation at CZD where the range was shown to be 18.2%–50% with an average of 32.2% (White et al. 2015), suggesting that the 2015/16 and 2016/17 wet seasons were normal at CZD. However, White et al. (2015) showed a 21.9% seasonal NBB_{50} rain average at STR and we observed higher percentages of 27.7% and 30.7%, suggesting higher than previously observed seasonal NBB rain in the valley. The percentages observed in the Northern Coast Ranges are higher than observed in Oregon and Washington, the southeastern United States, and similar to observed on the Chilean Coast and the Sierra Nevada downstream of terrain gaps (Neiman et al. 2005; White et al. 2015; Matrosov et al. 2016; Massmann et al. 2017; Zagrodnik et al. 2018).

NBB_{50} rain at HOP was much lower than STR in the average rain rate and seasonal percentages (Figs. 2, 3, 6, 7). Upwind (230°) of STR are small hills that range from 100 to 300 m MSL, while upwind of HOP are mountains that exceed 1 km MSL (Fig. 1). Less moisture is removed from the air when it travels through gaps in terrain compared to being lifted and precipitating out over mountains (e.g., Smith et al. 2010; White et al. 2015). Therefore, the Petaluma Gap may allow for higher NBB rain in the southern Russian River Valley (e.g., STR; Fig. 1). Whereas it is possible that HOP observes a rain shadow due to descending air into the Upper Russian River Valley similar to the Santa Clara Valley to the south, given the higher upwind terrain (Behringer and Chaio 2019).

The low-GE events had echo tops that rarely extend above the freezing level suggesting pure warm rain whereas all high-GE events had echo tops above the freezing level where ice may be present (Fig. 10). Further, the CFADs demonstrated that growth from mixed-phase processes were crucial for heavy NBB_{20} rain and had twofold effect. Mixed-phase processes led to rapid growth in hydrometeor size near the echo top as evidenced by rapid increases in pseudoreflectivity, and continued growth below the freezing level, likely from a broadening in the DSD that is not observed in low-GE rain. An example of low- and high-GE NBB rain and observed DSDs are shown in

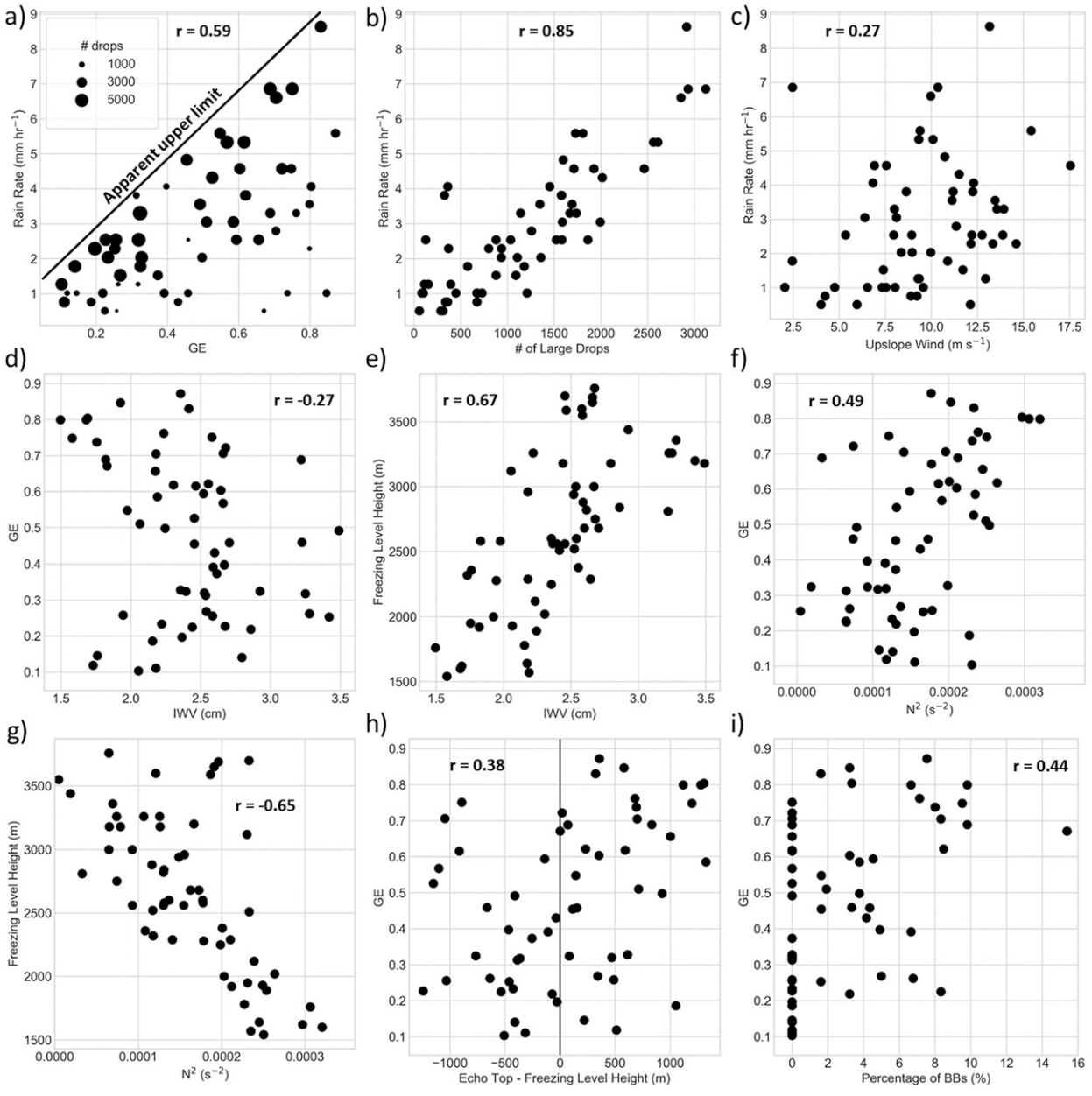

FIG. 13. Scatterplots for NBB_{20} rain rate and atmospheric variables when echo tops are between 2.5 and 3 km MSL at MDT ($N = 58$). All correlation coefficients are statistically significant ($p < 0.05$). All heights are shown in MSL.

Fig. 14. Low-GE NBB rain exhibits the largest increases in SNR near the surface and a larger quantity of small drops (Figs. 14a,b). High-GE NBB rain shows rapid increase in SNR near the echo top, above the freezing level, and higher SNR toward the surface than low-GE as well as fewer small drops and more large drops (Figs. 14c,d). DSDs of low-GE ($GE_{0–0.25}$; Fig. 9) are similar to the ''large quantities of small drops'' regime in Zagrodnik et al. (2018), which occurred with higher than average freezing levels. Our analysis showed this regime with lower echo tops that rarely extended above the freezing level (Fig. 10). DSDs of high-GE ($GE_{0.75–1}$; Fig. 9) are similar to the ''smaller quantities of large drops'' regime in Zagrodnik et al. (2018) from lower freezing levels and mixed-phase processes.

Given the marginal extension of echo tops beyond the freezing level in the high-GE NBB_{20} rain (0–1.5 km above freezing level), temperatures near the top of the precipitating cloud would theoretically only be 0°–7.5°C below freezing in 5°C km^{-1} moist adiabatic ascent. These are very warm temperatures for ice, but theoretically possible as shown by (Wilson et al. 2015; DeMott et al. 2016; Ladino et al. 2016; Kanji et al. 2017 and references therein). The data presented

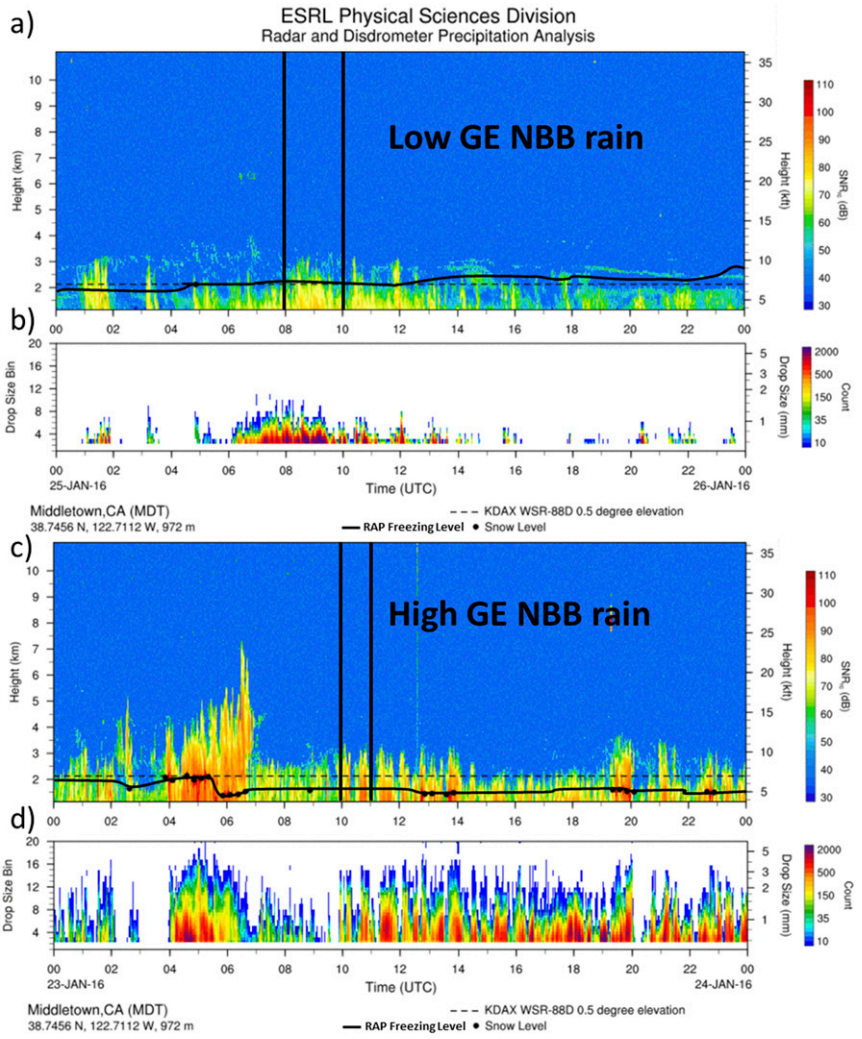

FIG. 14. (a) S-PROF SNR vertical profile for 25 Jan 2016 precipitation event at MDT. Hours between the black bars comprise part of the $GE_{0–0.25}$ sample shown in Fig. 11a. (b) DSD associated with (a). (c) S-PROF SNR vertical profile for 23 Jan 2016 precipitation event at MDT. Hour between the black bars comprise part of the $GE_{0.75–1}$ sample shown in Fig. 11b. (d) DSD associated with (c). Black lines show the approximate RAP freezing level height; black dots show snow level height when detected. Heights are shown in MSL. Images provided by the NOAA Physical Sciences Laboratory, Boulder, Colorado, from their website at https://psl.noaa.gov/.

herein suggest that ice does occur in shallow maritime precipitation with relatively warm tops and is more important than may have been previously considered or alluded to (e.g., Kingsmill et al. 2016; Massmann et al. 2017), especially for the heaviest NBB rain intensities. Improved measurements of ice in NBB rain clouds are imperative to further study the role of ice in NBB rain beyond this analysis. Additionally, further study must be conducted using cloud tops rather than echo tops to better understand the depth of the cloud above the freezing level.

6. Conclusions

This paper presents a comprehensive study of NBB rain at two mountain and two valley sites in the Northern Coast Ranges of California during the 2016 and 2017 water years. We investigated seasonal contributions of NBB rain at each site and the frequency of NBB rain rates. An atmospheric forcing site was used to determine the controls on NBB rain rates and their frequency. Additionally, the metric of growth efficiency (GE), defined by disdrometer data, was presented to separate microphysical growth environments that lead to light or heavy NBB rain rates and to understand the role of echo top height and ice in producing heavy NBB rain. The main findings are as follows:

- NBB rain is not the same as warm rain as previously stated in the literature. Rainfall occurs without any bright bands in only 32%–46% of NBB rain in our analysis depending on location.

- NBB_0 is the closest radar-derived approximation to pure warm rain, but ice cannot be ruled out if the echo top is above the freezing level. NBB_0 rain rates were $<5\,mm\,h^{-1}$ in the valleys and $<10\,mm\,h^{-1}$ at mountain sites whereas rain rates as high as 17 and 22 $mm\,h^{-1}$ were observed for NBB_{20} and NBB_{50}, respectively. Mixed-phase clouds are therefore paramount for heavy NBB rain rates as a primary source for flooding events.
- Mixed-phase processes can occur with echo tops < 1 km above the freezing level which increase the efficiency of hydrometeor growth. Mixed-phase processes lead to a broader DSD which may also improve the efficiency of coalescence below the freezing level.
- NBB rain rates and seasonal contribution from NBB rain varied substantially in the Northern Coast Ranges. STR observed heavier average NBB rain rates and seasonal NBB rain than the other valley site, HOP, possibly due to higher terrain upwind of HOP causing a rain shadow effect as air descends into the Northern Russian River Valley. MDT observed more frequent, heavier average intensity, and more seasonal NBB rain than CZD, likely due to the higher mountain elevation.

Because NBB rain can contain ice-phase hydrometeors, it is not suggested to be used to differentiate between warm rain and ice-initiated rain. However, the distinction between NBB and BB rain does provide meaningful information on the microphysical processes by 1) identifying precipitating systems which do not contain sufficient populations of large melting ice crystals to produce a bright band, and 2) offering a technique to quantify the role of mixed-phase processes via the number of bright bands detected in a given time period. Additionally, NBB rain is distinctly different from BB rain as it is often a shallow, orographic process characterized by larger populations of smaller drops. These properties make it difficult to estimate NBB rain rate with operational scanning radar, and, thus, it is a useful precipitation type for research and operational purposes.

Acknowledgments. We thank three anonymous reviewers for their feedback to substantially improve the quality of this manuscript. This work was completed as part of the National Oceanic and Atmospheric Administration (NOAA) Pathways Student Internship Program. The data used in this study were collected by the NOAA's Earth System Laboratory (ESRL) Hydrometeorology Testbed (HMT; http://hmt.noaa.gov/), and we thank everyone involved in collecting and maintaining the data.

REFERENCES

Behringer, D., and S. Chaio, 2019: Numerical investigations of atmospheric rivers and the rain shadow over the Santa Clara Valley. *Atmosphere*, **10**, 114, https://doi.org/10.3390/atmos10030114.

Bevis, M., S. Businger, T. A. Herring, C. Rocken, R. A. Anthes, and R. H. Ware, 1992: GPS meteorology: Remote sensing of atmospheric water vapor using the global positioning system. *J. Geophys. Res.*, **97**, 15 787–15 801, https://doi.org/10.1029/92JD01517.

Coplen, T. B., P. J. Neiman, A. B. White, and F. M. Ralph, 2015: Categorisation of northern California rainfall for periods with and without a radar brightband using stable isotopes and a novel automated precipitation collector. *Tellus*, **67B**, 28574, https://doi.org/10.3402/tellusb.v67.28574.

DeMott, P. J., and Coauthors, 2016: Sea spray aerosol as a unique source of ice nucleating particles. *Proc. Natl. Acad. Sci. USA*, **113**, 5797–5803, https://doi.org/10.1073/pnas.1514034112.

Dettinger, M. D., F. M. Ralph, T. Das, P. J. Neiman, and D. R. Cayan, 2011: Atmospheric Rivers, Floods and the Water Resources of California. *Water*, **3**, 445–478, https://doi.org/10.3390/w3020445.

Ecklund, W. L., C. R. Williams, P. E. Johnston, and K. S. Gage, 1999: A 3-GHz profiler for precipitating cloud studies. *J. Atmos. Oceanic Technol.*, **16**, 309–322, https://doi.org/10.1175/1520-0426(1999)016<0309:AGPFPC>2.0.CO;2.

Feingold, G., W. R. Cotton, S. M. Kreidenweis, and J. T. Davis, 1999: The impact of giant cloud condensation nuclei on drizzle formation in stratocumulus: Implications for cloud radiative properties. *J. Atmos. Sci.*, **56**, 4100–4117, https://doi.org/10.1175/1520-0469(1999)056<4100:TIOGCC>2.0.CO;2.

Franklin, C. N., 2008: A warm rain microphysics parameterization that includes the effect of turbulence. *J. Atmos. Sci.*, **65**, 1795–1816, https://doi.org/10.1175/2007JAS2556.1.

Friedrich, K., E. A. Kalina, J. Aikins, M. Steiner, D. Gochis, P. A. Kucera, K. Ikeda, and J. Sun, 2016: Raindrop size distribution and rain characteristics during the 2013 Great Colorado Flood. *J. Hydrometeor.*, **17**, 53–72, https://doi.org/10.1175/JHM-D-14-0184.1.

Grossi, G., A. Lendvai, G. Perretti, and R. Ranzi, 2017: Snow precipitation measured by gauges: Systematic error estimation and data series correction in the central Italian Alps. *Water*, **9**, 461, https://doi.org/10.3390/w9070461.

Guerova, G., E. Brockmann, J. Quiby, F. Schubiger, and C. Matzler, 2003: Validation of NWP mesoscale models with Swiss GPS network AGNES. *J. Appl. Meteor.*, **42**, 141–150, https://doi.org/10.1175/1520-0450(2003)042<0141:VONMMW>2.0.CO;2.

Hughes, M., A. Hall, and R. G. Fovell, 2009: Blocking in areas of complex topography, and its influence on rainfall distribution. *J. Atmos. Sci.*, **66**, 508–518, https://doi.org/10.1175/2008JAS2689.1.

Jensen, J. B., and A. D. Nugent, 2017: Condensational growth of drops formed on giant sea-salt aerosol particles. *J. Atmos. Sci.*, **74**, 679–697, https://doi.org/10.1175/JAS-D-15-0370.1.

Johnson, D. B., 1982: The role of giant and ultragiant aerosol particles in warm rain initiation. *J. Atmos. Sci.*, **39**, 448–460, https://doi.org/10.1175/1520-0469(1982)039<0448:TROGAU>2.0.CO;2.

Joss, J., and A. Waldvogel, 1967: Ein spektrograph für niederschlagstropfen mit automatischer auswertung. *Pure Appl. Geophys.*, **68**, 240–246, https://doi.org/10.1007/BF00874898.

Kanji, Z. A., L. A. Ladino, H. Wex, Y. Boose, M. Burkert-Kohn, D. J. Cziczo, and M. Krämer, 2017: Overview of ice nucleating particles. *Ice Formation and Evolution in Clouds and Precipitation: Measurement and Modeling Challenges*, *Meteor. Monogr.*, No. 58, Amer. Meteor. Soc., https://doi.org/10.1175/AMSMONOGRAPHS-D-16-0006.1.

Kingsmill, D. E., P. J. Neiman, F. M. Ralph, and A. B. White, 2006: Synoptic and topographic variability of northern California precipitation characteristics in landfalling winter storms observed during CALJET. *Mon. Wea. Rev.*, **134**, 2072–2094, https://doi.org/10.1175/MWR3166.1.

——, ——, and A. B. White, 2016: Microphysics regime impacts on the relationship between orographic rain and orographic forcing in the coastal mountains of Northern California.

J. Hydrometeor., **17**, 2905–2922, https://doi.org/10.1175/JHM-D-16-0103.1.

Kirshbaum, D. J., and R. B. Smith, 2008: Temperature and moist-stability effects on midlatitude orographic precipitation. *Quart. J. Roy. Meteor. Soc.*, **134**, 1183–1199, https://doi.org/10.1002/qj.274.

Kochendorfer, J., and Coauthors, 2017: The quantification and correction of wind-induced precipitation measurement errors. *Hydrol. Earth Syst. Sci.*, **21**, 1973–1989, https://doi.org/10.5194/hess-21-1973-2017.

Korolev, A. V., and I. P. Mazin, 2003: Supersaturation of water vapor in clouds. *J. Atmos. Sci.*, **60**, 2957–2974, https://doi.org/10.1175/1520-0469(2003)060<2957:SOWVIC>2.0.CO;2.

Ladino, L. A., and Coauthors, 2016: Addressing the ice nucleating abilities of marine aerosol: A combination of deposition mode laboratory and field measurements. *Atmos. Environ.*, **132**, 1–10, https://doi.org/10.1016/j.atmosenv.2016.02.028.

Li, G., and J. Deng, 2013: Atmospheric water monitoring by using ground-based GPS during heavy rains produced by TPV and SWV. *Adv. Meteor.*, **2013**, 793957, https://doi.org/10.1155/2013/793957.

Lund, J., J. Medellin-Azuara, J. Durand, and K. Stone, 2018: Lessons from California's 2012-2016 drought. *J. Water Resour. Plann. Manage.*, **144**, 04018067, https://doi.org/10.1061/(ASCE)WR.1943-5452.0000984.

Martner, B. E., and Coauthors, 1993: An evaluation of wind profiler, RASS, and microwave radiometer performance. *Bull. Amer. Meteor. Soc.*, **74**, 599–614, https://doi.org/10.1175/1520-0477(1993)074<0599:AEOWPR>2.0.CO;2.

——, S. E. Yuter, A. B. White, S. Y. Matrosov, D. E. Kingsmill, and F. M. Ralph, 2008: Raindrop size distributions and rain characteristics in California coastal rainfall for periods with and without a radar bright band. *J. Hydrometeor.*, **9**, 408–425, https://doi.org/10.1175/2007JHM924.1.

Massmann, A. K., J. R. Minder, R. D. Garreaud, D. E. Kingsmill, R. A. Valenzuela, A. Montecinos, S. L. Fults, and J. R. Snider, 2017: The Chilean coastal orographic precipitation experiment: Observing the influence of microphysical rain regimes on coastal orographic precipitation. *J. Hydrometeor.*, **18**, 2723–2743, https://doi.org/10.1175/JHM-D-17-0005.1.

Matrosov, S. Y., F. M. Ralph, P. J. Neiman, and A. B. White, 2014: Quantitative assessment of operational weather radar rainfall estimates over California's Northern Sonoma County using HMT-West data. *J. Hydrometeor.*, **15**, 393–410, https://doi.org/10.1175/JHM-D-13-045.1.

——, R. Cifelli, P. J. Neiman, and A. B. White, 2016: Radar rainrate estimators and their variability due to rainfall type: An assessment based on hydrometeorology testbed data from the southeastern United States. *J. Appl. Meteor. Climatol.*, **55**, 1345–1358, https://doi.org/10.1175/JAMC-D-15-0284.1.

Mattioli, V., E. R. Westwater, D. Cimini, J. C. Liljegren, B. M. Lesht, S. I. Gutman, and F. J. Schmidlin, 2007: Analysis of radiosonde and ground-based remotely sensed PWV data from the 2004 north slope of Alaska Arctic winter radiometric experiment. *J. Atmos. Oceanic Technol.*, **24**, 415–431, https://doi.org/10.1175/JTECH1982.1.

May, P. T., R. G. Strauch, and K. P. Moran, 1988: The altitude coverage of temperature measurements using RASS with wind profiler radars. *Geophys. Res. Lett.*, **15**, 1381–1384, https://doi.org/10.1029/GL015i012p01381.

——, K. P. Moran, and R. G. Strauch, 1989: The accuracy of RASS temperature measurements. *J. Appl. Meteor.*, **28**, 1329–1335, https://doi.org/10.1175/1520-0450(1989)028<1329:TAORTM>2.0.CO;2.

Neiman, P. J., F. M. Ralph, A. B. White, D. E. Kingsmill, and P. O. Persson, 2002: The statistical relationship between upslope flow and rainfall in California's coastal mountains: Observations during CALJET. *Mon. Wea. Rev.*, **130**, 1468–1492, https://doi.org/10.1175/1520-0493(2002)130<1468:TSRBUF>2.0.CO;2.

——, G. A. Wick, F. M. Ralph, B. E. Martner, A. B. White, and D. E. Kingsmill, 2005: Wintertime nonbrightband rain in California and Oregon during CALJET and PACJET: Geographic, interannual, and synoptic variability. *Mon. Wea. Rev.*, **133**, 1199–1223, https://doi.org/10.1175/MWR2919.1.

——, A. B. White, F. M. Ralph, D. J. Gottas, and S. I. Gutman, 2009: A water vapor flux tool for precipitation forecasting. *Proc. Inst. Civ. Eng.-Water Manage.*, **162**, 83–94, https://doi.org/10.1680/wama.2009.162.2.83.

——, D. J. Gottas, A. B. White, L. J. Schick, and F. M. Ralph, 2014: The use of snow-level observations derived from vertically profiling radars to assess hydrometeorological characteristics and forecasts over Washington's green river basin. *J. Hydrometeor.*, **15**, 2522–2541, https://doi.org/10.1175/JHM-D-14-0019.1.

NOAA/NCEI, 2017: Rapid Refresh (RAP), 13 km. NOAA Operational Model Archive and Distribution System, accessed 19 November 2017, https://www.ncdc.noaa.gov/data-access/model-data/model-datasets/rapid-refresh-rap.

NOAA/PSL, 2017: Profiler Network Data and Image Library. Physical Sciences, Laboratory, accessed 18 October 2017, https://psl.noaa.gov/data/obs/datadisplay/.

Pollock, M. D., and Coauthors, 2018: Quantifying and mitigating wind-induced undercatch in rainfall measurements. *Water Resour. Res.*, **54**, 3863–3875, https://doi.org/10.1029/2017WR022421.

Posselt, R., and U. Lohmann, 2008: Influence of giant CCN on warm rain processes in the ECHAM5 GCM. *Atmos. Chem. Phys.*, **8**, 3769–3788, https://doi.org/10.5194/acp-8-3769-2008.

Ralph, F. M., P. J. Neiman, G. A. Wick, S. I. Gutman, M. D. Dettinger, D. R. Cayan, and A. B. White, 2006: Flooding on California's Russian River: Role of atmospheric rivers. *Geophys. Res. Lett.*, **33**, L13801, https://doi.org/10.1029/2006GL026689.

Rasmussen, R., and Coauthors, 2012: How well are we measuring snow: The NOAA/FAA/NCAR winter precipitation test bed. *Bull. Amer. Meteor. Soc.*, **93**, 811–829, https://doi.org/10.1175/BAMS-D-11-00052.1.

Rosen, J., 2017: California rain put spotlight on atmospheric rivers. *Science*, **355**, 787, https://doi.org/10.1126/science.355.6327.787.

Ryoo, J.-M., and Coauthors, 2020: Terrain trapped airflows and precipitation variability during an atmospheric river event. *J. Hydrometeor.*, **21**, 355–375, https://doi.org/10.1175/JHM-D-19-0040.1.

Sheppard, B. E., and P. I. Joe, 1994: Comparison of raindrop size distribution measurements by a Joss–Waldvogel disdrometer, a PMS 2DG spectrometer, and a POSS Doppler radar. *J. Atmos. Oceanic Technol.*, **11**, 874–887, https://doi.org/10.1175/1520-0426(1994)011<0874:CORSDM>2.0.CO;2.

Sieck, L. C., S. J. Burges, and M. Steiner, 2007: Challenges in obtaining reliable measurements of point rainfall. *Water Resour. Res.*, **43**, W01420, https://doi.org/10.1029/2005WR004519.

Smith, B. L., S. E. Yuter, P. J. Neiman, and D. E. Kingsmill, 2010: Water vapor fluxes and orographic precipitation over northern California associated with a landfalling atmospheric river. *Mon. Wea. Rev.*, **138**, 74–100, https://doi.org/10.1175/2009MWR2939.1.

Song, N., and J. Marwitz, 1989: A numerical study of the warm rain process in orographic clouds. *J. Atmos. Sci.*, **46**, 3479–3486,

https://doi.org/10.1175/1520-0469(1989)046<3479:ANSOTW>2.0.CO;2.

Szumowski, M. J., R. M. Rauber, H. T. Ochs, and L. J. Miller, 1997: The microphysical structure and evolution of Hawaiian rainband clouds. Part I: Radar observations of rainbands containing high reflectivity cores. *J. Atmos. Sci.*, **54**, 369–385, https://doi.org/10.1175/1520-0469(1997)054<0369:TMSAEO>2.0.CO;2.

Valenzuela, R., and D. E. Kingsmill, 2018: Terrain-trapped airflows and orographic rainfall along the cost of Northern California. Part II: Horizontal and vertical structures observed by a scanning Doppler radar. *Mon. Wea. Rev.*, **146**, 2381–2402, https://doi.org/10.1175/MWR-D-17-0227.1.

Wallace, J. M., and P. V. Hobbs, 2006: *Atmospheric Science: An Introductory Survey*. Elsevier Academic Press, 483 pp.

Weber, B. L., D. B. Wuertz, D. C. Welsh, and R. McPeek, 1993: Quality controls for profiler measurements of winds and RASS temperatures. *J. Atmos. Oceanic Technol.*, **10**, 452–464, https://doi.org/10.1175/1520-0426(1993)010<0452:QCFPMO>2.0.CO;2.

White, A. B., J. R. Jordan, B. E. Martner, F. Martin Ralph, and B. W. Bartram, 2000: Extending the dynamic range of an S-band radar for cloud and precipitation studies. *J. Atmos. Oceanic Technol.*, **17**, 1226–1234, https://doi.org/10.1175/1520-0426(2000)017<1226:ETDROA>2.0.CO;2.

——, D. J. Gottas, E. T. Strem, F. M. Ralph, and P. J. Neiman, 2002: An automated brightband height detection algorithm for use with Doppler radar spectral moments. *J. Atmos. Oceanic Technol.*, **19**, 687–697, https://doi.org/10.1175/1520-0426(2002)019<0687:AABHDA>2.0.CO;2.

——, P. J. Neiman, F. M. Ralph, D. E. Kingsmill, and P. O. Persson, 2003: Coastal orographic rainfall processes observed by radar during the California Land-Falling Jets Experiment. *J. Hydrometeor.*, **4**, 264–282, https://doi.org/10.1175/1525-7541(2003)4<264:CORPOB>2.0.CO;2.

——, D. J. Gottas, A. F. Henkel, P. J. Neiman, F. M. Ralph, and S. I. Gutman, 2010: Developing a performance measure for snow-level forecasts. *J. Hydrometeor.*, **11**, 739–753, https://doi.org/10.1175/2009JHM1181.1.

——, and Coauthors, 2013: A twenty-first-century California observing network for monitoring extreme weather events. *J. Atmos. Oceanic Technol.*, **30**, 1585–1603, https://doi.org/10.1175/JTECH-D-12-00217.1.

——, P. J. Neiman, J. M. Creamean, T. Coleman, F. M. Ralph, and K. A. Prather, 2015: The impacts of California's San Francisco Bay area gap on precipitation observed in the Sierra Nevada during HMT and CalWater. *J. Hydrometeor.*, **16**, 1048–1069, https://doi.org/10.1175/JHM-D-14-0160.1.

Whiteman, C. D., 2000: *Mountain Meteorology: Fundamentals and Applications*. Oxford University Press, 355 pp.

Wilson, T. W., and Coauthors, 2015: A marine biogenic source of atmospheric ice-nucleating particles. *Nature*, **525**, 234–238, https://doi.org/10.1038/nature14986.

Wolfe, D. E., and S. I. Gutman, 2000: Developing an operational, surface-based, GPS, water vapor observing system for NOAA: Network design and results. *J. Atmos. Oceanic Technol.*, **17**, 426–440, https://doi.org/10.1175/1520-0426(2000)017<0426:DAOSBG>2.0.CO;2.

Yuter, S. E., and R. A. Houze, 1995: Three-dimensional kinematic and microphysical evolution of Florida cumulonimbus. Part II: Frequency distributions of vertical velocity, reflectivity, and differential reflectivity. *Mon. Wea. Rev.*, **123**, 1941–1963, https://doi.org/10.1175/1520-0493(1995)123<1941:TDKAME>2.0.CO;2.

Zagrodnik, J. P., L. A. McMurdie, and R. A. Houze, 2018: Stratiform precipitation processes in cyclones passing over a coastal mountain range. *J. Atmos. Sci.*, **75**, 983–1004, https://doi.org/10.1175/JAS-D-17-0168.1.

——, ——, ——, and S. Tanelli, 2019: Vertical structure and microphysical characteristics of frontal systems passing over a three-dimensional coastal mountain range. *J. Atmos. Sci.*, **76**, 1521–1546, https://doi.org/10.1175/JAS-D-18-0279.1.

Zhang, L. M., D. V. Michelangeli, and P. A. Taylor, 2006: Influence of aerosol concentration on precipitation formation in low-level, warm stratiform clouds. *J. Aerosol Sci.*, **37**, 203–217, https://doi.org/10.1016/j.jaerosci.2005.04.002.